Measurement of direct-contact condensation of pure saturated vapour on an injection spray by applying pulsed laser holography†

F. MAYINGER and A. CHÁVEZ

Lehrstuhl A für Thermodynamik, Technische Universität München, Arcisstr. 21,
8000 München 2, Germany

Abstract—An application of pulsed laser holography for direct measurement of the growth of subcooled spray droplets in a pure saturated vapour is presented. The spray flow corresponds to intermediate and high droplet Reynolds numbers ($100 \leqslant Re \leqslant 3500$) while the vapour pressure is varied in a wide range of reduced pressures ($0.03 \leqslant p_r \leqslant 0.3$). The holographic reconstructions reveal a strong relation between the vapour pressure and the spray geometry. At moderate liquid flow rate and relatively high vapour pressure, subsequent pressure increments produce dramatic changes in the spray geometry and considerably reduce the condensation rate.

INTRODUCTION

CONDENSATION of vapour on spray droplets has recently been the subject of several detailed studies [1–5]. The reason for this interest lies in the numerous application possibilities of sprays in many fields of the chemical industries and power engineering; with particular regard to the design of mixing-type heat exchangers, direct-contact condensers in geothermal power plants, air conditioning humidifiers and emergency core cooling in nuclear power plants. For scientists the transport phenomena to the direct-contact condensation are of great interest too, because the mechanisms of heat, momentum and mass transfer at the interface between drops and their gaseous environment have not been completely cleared. In this sense, there are many theoretical, as well as experimental, studies in the literature describing the hydrodynamics of drops in condensable environment [6, 7], the growth rate of a single drop in pure vapour [8] or in air–steam mixtures [9, 10], and condensation rates on drops moving at low Reynolds numbers [11, 12], at intermediate Reynolds numbers [6, 7] and at high Reynolds numbers [13, 14]. Numerical procedures to solve the condensation problem associated with single droplets are also available [7, 15].

In spite of all these efforts, there is still a lack of experimental data regarding the spray behaviour when the reduced pressure $p_r = p_v/p_c$ of the vapour fraction in the gaseous environment is higher than 0.03. This situation leads to serious errors in dimensioning equipment or in process controlling as pointed out by De Corso and Kemeny [16]. Therefore, it is necessary to provide experimental evidence on the

behaviour of injection sprays in a high-pressure condensable atmosphere.

This work presents experimental results of a large investigation programme on the condensation of pure saturated vapour on subcooled liquid hollow-cone sprays of the same substance as the vapour, covering a range of reduced pressures up to one order of magnitude higher than before. The model fluid, refrigerant R113 (trifluorotrichloroethane), is injected through a 60° pressure-swirl nozzle of 0.6 mm in bore diameter at different mass flow rates $\dot{M}$ (0.8–3.86 g s^{-1}), which correspond to droplet flows in the range of intermediate, $Re = O(100)$, and high Reynolds numbers, $Re = O(1000)$. The work also presents a complete characterization of the spray flow, which could be carried out by applying off-axis pulsed laser holography. Special emphasis is given to the discussion of the effect of raising the vapour pressure on the behaviour of the spray, and hence on the condensation rate.

PHYSICAL DESCRIPTION AND SCOPE

The spray flow

In a pressure-swirl nozzle the liquid is conducted through spiral-like channels that discharge it tangentially into a vortex or swirl chamber, from which it is injected into the gaseous environment. The emerging liquid possesses both tangential, radial and axial momentum components which extend it to form a thin conical sheet at the nozzle outlet. Under the action of destabilizing forces (inertial and aerodynamic forces) this sheet rapidly breaks up into ligaments, drop chains and finally into drops. The disintegration process is highly irregular producing drops of different diameters and velocities [17]. Therefore, the spray can be handled as a droplet spectrum with both diameters (D) and velocities (U) varying around a mean value

---

† Dedicated to Professor Dr.-Ing. Dr.-Ing.e.h. Ulrich Grigull.

NOMENCLATURE

A	surface	p_v	vapour pressure
c_p	specific heat of the liquid	$\dot{R}$	time-resolved droplet growth
D	drop diameter	Re	droplet Reynolds number $Re = \rho_v \bar{U} \bar{D}/\eta_v$
δD	relative droplet growth	r, z, ϕ	cylindrical coordinates (Fig. 1)
D_{32}	Sauter mean diameter	S	standard deviation
d_0	nozzle bore diameter	T	temperature
h_{fg}	latent heat of vaporization	t	time
h_D	heat transfer coefficient at the droplet collective	U	drop velocity
		X, Y, Z	cartesian coordinates (Fig. 3).
h_S	heat transfer coefficient at the liquid sheet		
Ja	Jakob number $Ja = \rho c_p (T_{sat} - T_0)/\rho_v h_{fg}$		
L_z	break up length	**Greek symbols**	
$\dot{M}$	mass flow rate	α	spray angle
$\dot{M}_S$	condensation rate at the liquid sheet	δ	thickness of the liquid sheet
N	droplet number	η_v	dynamic viscosity of the vapour
Nu	Nusselt number $Nu = h_D \bar{D}/\lambda$	λ	heat conductivity of the liquid
p_c	critical pressure	ρ	liquid density
p_r	reduced pressure $p_r = p_v/p_c$	ρ_v	vapour density.

$\bar{D}$ and $\bar{U}$ respectively. The final distribution of the droplets in the injection chamber, and hence the general performance of the spray, depends very strongly on the form of the liquid sheet (shape and break up length) as observed by several experimentalists (e.g. see refs. [2, 17, 18]). Therefore, measurements of the liquid sheet geometry are of special interest for this work.

Figure 1 shows a scheme of the spray flow. Here, r and z are axis symmetrical, cylindrical coordinates with origin O at the nozzle outlet. α is the spray angle and L_z is the distance at which the continuous liquid sheet of the spray breaks up in a droplet swarm. Together with the sheet thickness δ, they characterize the liquid sheet geometry. The liquid is injected at an initial temperature T_0 into its own saturated vapour. The vapour lies initially in repose and its temperature $T_{sat} > T_0$ is maintained constant. At steady state conditions, and assuming a temperature field with axial symmetry, the bulk liquid temperature T can be expressed as a function of the axial coordinate z. At $z = z_k$ the droplets are supposed to have reached the temperature, T_{sat}, of the saturated vapour environ-

ment. One identifies in Fig. 1 the conical liquid sheet, the break up zone or zone of ligaments and drop chains and the droplet zone. Although the break up zone extends only a few nozzle diameters in the axial direction, a great activity for heat and mass exchange reigns in it. For this reason special emphasis should be put on distinguishing this zone from that in which the droplets are fully developed if comparisons of our measurements with theoretical predictions are wanted.

MEASURING TECHNIQUE

Pulsed laser holography

The pulsed laser holography represents one of the more suitable non-invasive measurement methods for the study of transport phenomena (e.g. heat and mass transfer) in dispersed transparent flows. It provides one or more three-dimensional scenes of the volume of interest taken at a very short exposure time (~ 30 ns). The recorded holograms can be reconstructed with the help of a continuous laser beam and analysed off-line at any time. Figure 2 shows the optical set-up
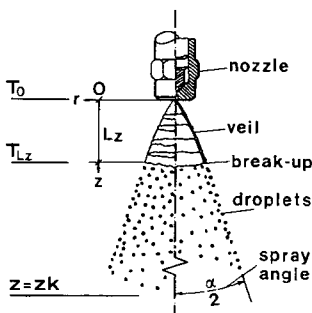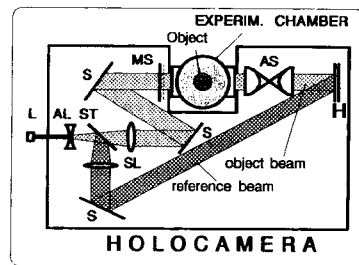

Fig. 1. Description of the spray flow.

Fig. 2. Holographic arrangement. (AL) divergent lens, (AS) imaging lens system, (H) holographic plate, (L) pulsed ruby laser, (MS) ground glass, (S) mirror, (SL) convergent lens and (ST) beam splitter.

for the recording of off-axis holograms. Using a separated reference beam, the holographic reconstructions can be observed directly or with help of a microscope as in a photograph. The reconstructed images are very clear for particle sizes $D > 10\lambda$, where D and λ are the drop diameter and the wavelength of the laser light used to record the hologram, respectively.

The laser L, schematically shown in Fig. 2, used to record the holograms is a pulsed ruby laser which produces light pulses of 1 Joule in a very short time of 30 ns. It can be operated in single or in double pulse modus. In single pulse modus the resulting holograms (single pulsed holograms) are very clear. They contain information about the geometry of the spray, the break up of the liquid sheet, and the droplet distribution in the control volume. When the laser is operated in double pulse modus the resulting holograms reconstruct two scenes of the spray flow which provide information about the droplet velocities and trajectories. The interval between pulses can be varied from 1 to 800 μs. The principal features of the holographic method and some advanced adaptations are explained in detail in ref. [18].

Hologram evaluation

One of the principal problems appearing in the application of pulsed laser holography consists of handling the large amount of information contained in the holograms. Theoretically, holographic materials are able to store the information on position, texture and brightness of more than 10^6 particles per square millimeter. In this case, the droplet concentration is very much lower (less than 20 drops per cubic millimetre of reconstructed space). Nevertheless, one single hologram can contain information about position, size and velocity of many thousands of droplets. Comprehensive studies of the

characteristics of the droplets and their interactions with the gaseous environment necessarily require the help of computer-aided particle counting and measuring methods.

Figure 3 shows a scene of the components of a digital image processing system used to evaluate the holographic reconstructions. The hologram H is reconstructed by illumination with a continuous parallel beam from a He–Ne laser, which simulates the reference beam. The optical information contained in the reconstructed image I is scanned by the video camera K, and transmitted to the digitizer D. Here, the signal is transformed into digital information and is stored in the digitizer frame memory, in the form of an array of 512×512 picture elements (pixels) of 8 bits. The digitizer is directly connected to the host computer C by a 16 bit bus interface, allowing for fast communication. The processing of the digitized picture is then carried out by the host computer using the digitizer frame memory interactively, for pixel allocation. In order to visualize the information actually stored in the digitizer frame memory, a continuous RGB (false colour: red, green, blue) output signal is produced which can be observed on the graphics monitor M. Due to the fact that the video camera can only record two-dimensional (2-D) pictures, for example in the optical plane X–Z, it must be focussed stepwise along the depth coordinate Y in order to process the 3-D holographic image. In this manner, the 3-D holographic image is transformed into a series of many 2-D video pictures, which are then measured and classified. Examples of representative stages of the image processing are presented in the form of photographs in Fig. 4. Here, the photographs A to D show the focussing process. The nozzle is included for better orientation. A represents an original view from the holographic reconstruction
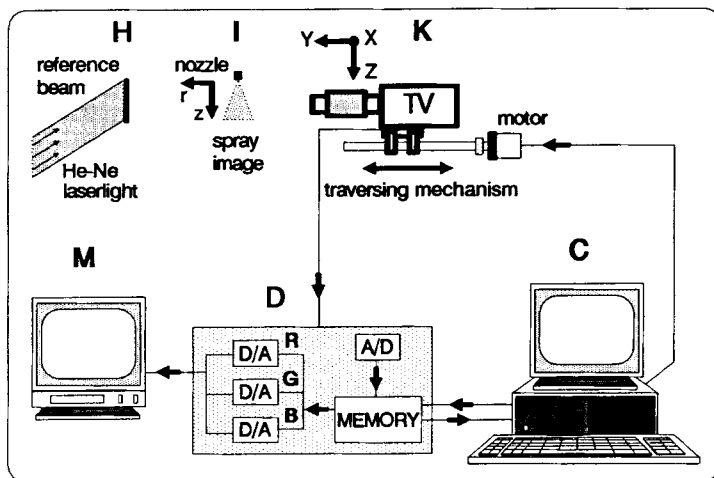

FIG. 3. Digital image processing system. (C) host computer, (D) digitizer, (H) hologram, (I) reconstructed spray image, (K) videocamera and (M) graphics monitor.
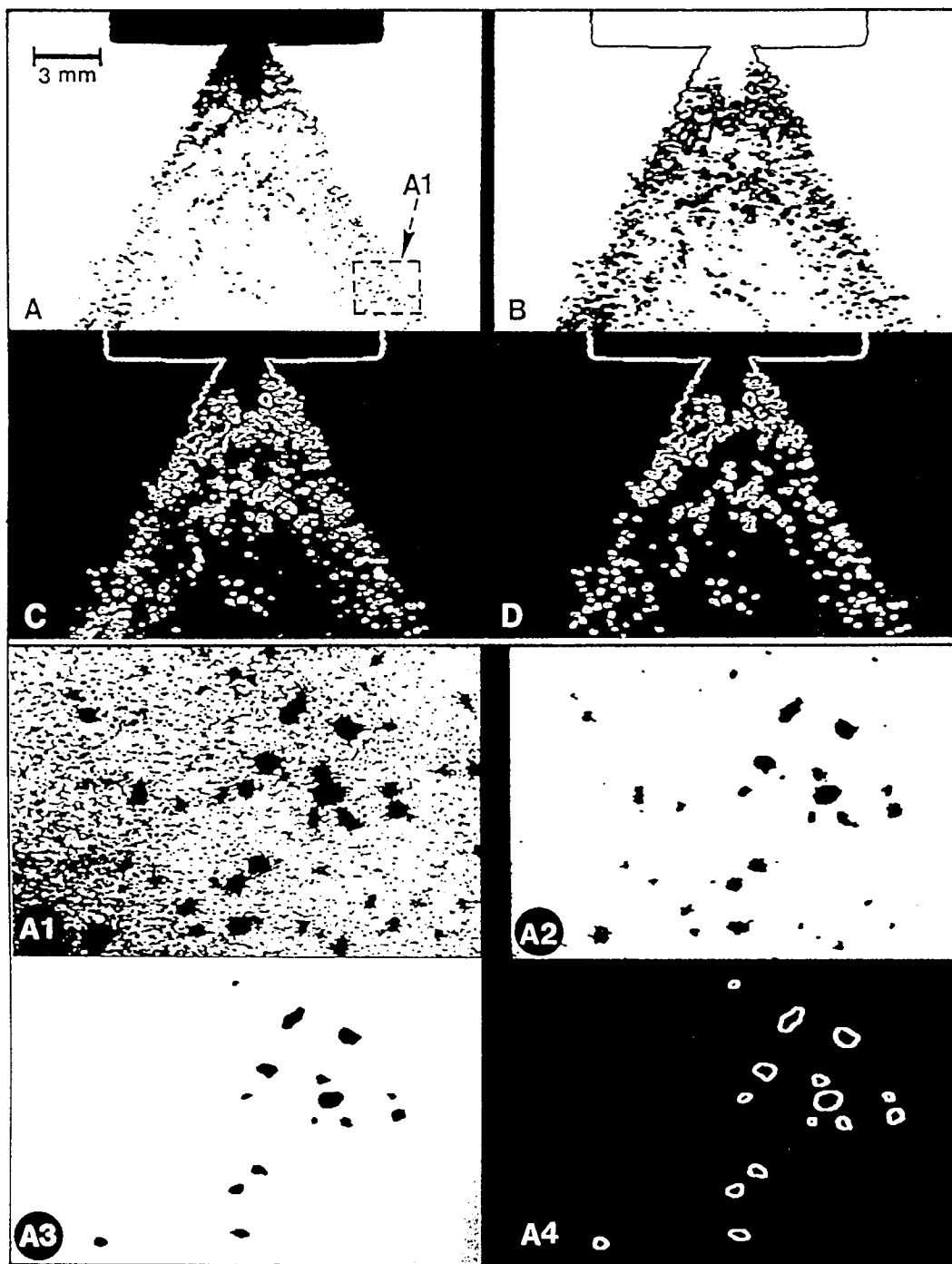
F. MAYINGER and A. CHÁVEZ

FIG. 4. Representative steps of the image processing of a single pulsed hologram of the R113 spray. (A) Original image, (B) smoothing and gradient extraction (C) binarization and (D) filtering. Picture (A1) shows an enlargement of the droplet zone of picture (A), its noise filtering process (A2) and (A3) and the final droplet identification in (A4).

and B to D successive filtering operations of A leading to a representation (D), which can be easily identified by the measuring algorithms. An enlargement A1 of the droplet zone of picture A is shown to illustrate the process of noise filtering (A2 to A4) and the final result in A4. A comprehensive description of hologram evaluations by applying digital image processing can be found in ref. [19].

EXPERIMENTS

The experiments were carried out in the autoclave presented schematically in Fig. 5. It consists of a thermally insulated cylindrical cavity of 206 mm interior diameter and 650 mm in height, designed for pressures up to 2 MPa. Two quartz glass windows (ϕ100 mm) installed in the cylindrical wall provide the optical access. The liquid is injected from the top of the vessel through the pressure-swirl nozzle. The nozzle, concentric with respect to the cylindrical wall, can be moved axially to permit the observation of any section of the spray. The lower third of the vessel is filled with liquid refrigerant R113 which is heated by an electrical resistance (1.2 kW) installed on the lower plenum, to produce the saturated vapour environment in the injection space of the autoclave. A funnel is placed between the boiling liquid and the spray to collect the spray droplets and to lead them to the outlet. Measurements of temperature and pressure at different points of interest in the facility were carried out by conventional thermocouples and pressure sensors monitored by a personal computer.

For a given nozzle and model fluid the spray parameters (i.e. L_z, α, δ) and the droplet size and velocity distributions depend only on the injected mass flow rate $\dot{M}$, on the degree of subcooling $\Delta T = T_{sat} - T_0$ and on the saturation pressure p_{sat} of the vapour atmosphere. In the present work, $\dot{M}$ and p_{sat} are systematically varied according to the experimental matrix shown in Table 1, while T_0 is directly measured·at the nozzle outlet. A description of temperature measurements on the spray were presented in ref. [20].
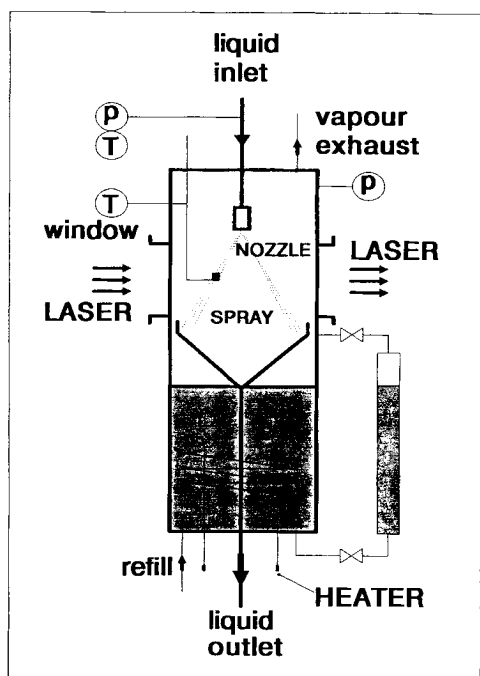

FIG. 5. Experimental chamber.

For each experiment the liquid mass flow rate $\dot{M}$ and the vapour pressure p_v are kept constant to provide steady state conditions. At each combination of $\dot{M}$ and p_v two hologram pairs were recorded. They correspond to the near and the far region of the spray with respect to the nozzle. Each hologram pair consists of a single and a double pulsed hologram. For the 40 combinations of $\dot{M}$ and p_v of the experimental matrix, a total of 160 holograms were recorded.

RESULTS AND DISCUSSION

Spray characterization

The diagrams of Figs. 6(a) and (b) summarize a great amount of measuring data (position, size and velocity of about two million droplets were stored) in the form of arithmetic mean values of drop diameters

$$\bar{D} = \frac{\sum\limits_{1}^{i} N_i D_i}{\sum\limits_{1} Ni} \qquad (1)$$

and velocities

$$\bar{U} = \frac{\sum\limits_{1}^{i} N_i U_i}{\sum\limits_{1} Ni} . \qquad (2)$$

The pressure p_v of the vapour environment is plotted as a parameter. In equations (1) and (2) the subindex i means a counter for the drop size classes and N the corresponding number of drops. The diagram of Fig. 6(a) shows an asymptotical decrease of the mean drop diameter $\bar{D}$ when the liquid mass flow rate is increased. According to Fraser and Eisenklam [17], the increase in the inertial forces, which depend on the flow rate, has a disintegrating effect upon the liquid sheet of the spray near the nozzle. This leads to the production of droplets with a smaller diameter. A direct influence of the variation of the vapour pressure upon the drop size could not be found. Figure 6(b) reveals that the mean drop velocity increases almost linearly with increasing liquid mass flow rate. In this case, the effect of varying the environmental pressure is clear. The mean drop velocity diminishes when the vapour pressure increases as would be expected, since the vapour density and viscosity also increase when the saturation pressure of the vapour increases. In both Figs. 6(a) and (b) the region of varicose break up is included for reference. The standard deviation S_D corresponding to the drop size measurements is included in Fig. 6(a). It depends only on the mass flow rate (i.e. on the droplet concentration). The higher the mass flow rate, the bigger the drop number, and hence the narrower the distribution curve. Regarding the velocity measurement, the standard deviation S_U behaves almost constant (between 3 and 5%) along the full range of mass flow rate. Its oscillations are completely

Table 1. Experimental matrix

$\dot{M}$ (g s^{-1})	p_v (MPa)							
	0.10	0.15	0.20	0.25	0.40	0.60	0.80	1.00
0.80	×	×	×	×	×	×	×	×
1.37	×	×	×	×	×	×	×	×
2.00	×	×	×	×	×	×	×	×
2.72	×	×	×	×	×	×	×	×
3.86	×	×	×	×	×	×	×	×

independent from both mass flow rate and vapour pressure (ref. [20], chap. 6).

As commented before, the liquid sheet geometry can be represented by the break up length L_z and the corresponding angle α at this length. The diagrams of

Figs. 7(a) and (b) present the measurements of L_z and α, respectively, as functions of the mass flow rate $\dot{M}$. The vapour pressure p_v is plotted again as a parameter. The diagram of Fig. 7(a) shows the typical decrease of the break up length when the mass flow rate, i.e. the sheer stress, is increased. The vapour pressure works like a reduction factor upon the shape of the curves up to a limit, after which the nozzle can no longer produce the hollow cone. Instead of that it works like a full cone nozzle. The explanation for this transition in the nozzle workwise is that at high reduced pressures $p_r = p_v/p_c$, the consequently high density and viscosity of the vapour of the vortex core in the nozzle swirl chamber produce a damping effect on the vortex intensity, which reduces the diameter of the vortex core. At subsequent increments of the vapour pressure the emerging liquid annulus at the
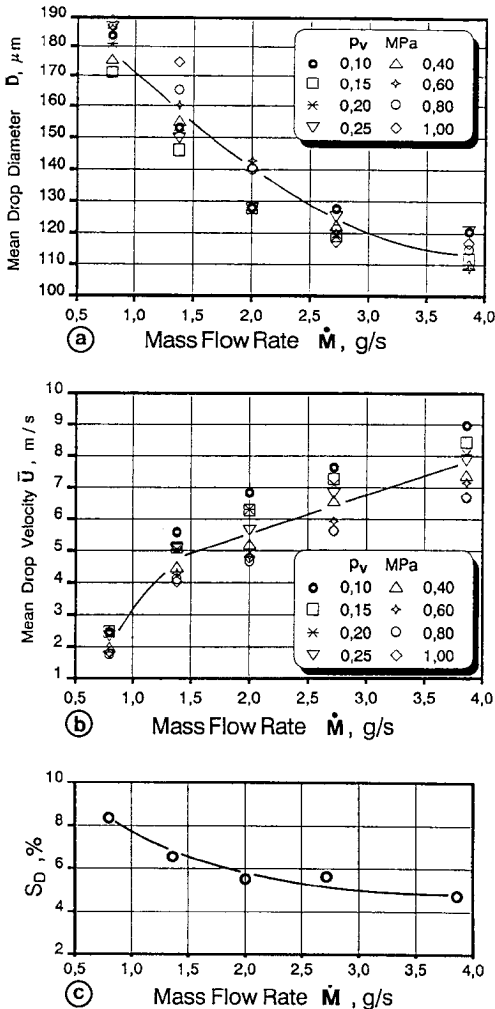

FIG. 6. (a) Mean drop size $\bar{D}$ and (b) mean drop velocity $\bar{U}$ as functions of the mass flow rate $\dot{M}$ of the R113 spray injected into its own saturated vapour at different vapour pressures p_v. (c) Standard deviation of the drop size measurements.
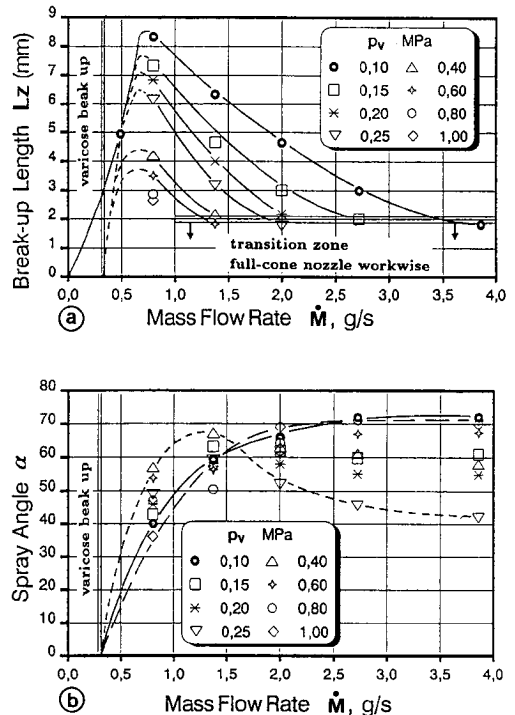

FIG. 7. (a) Break-up length L_z and (b) spray angle α as functions of the mass flow rate $\dot{M}$ of the R113 spray injected into its own saturated vapour at different vapour pressures p_v.

nozzle exit becomes thicker until a bottle-neck flow of high turbulence is produced. The tangential momentum of the liquid is no more than that needed to form the conical sheet. This situation leads to total contractions of the vapour core at the nozzle exit while the remaining vapour in the swirl chamber is compressed momentaneously and pushed out. The emerging vapour expands suddenly again contributing to the liquid atomization. This process repeats continuously producing the new nozzle workwise.

The change in the nozzle workwise is also evident in Fig. 7(b), in which the strong influence of the vapour pressure p_v upon the spray angle α is illustrated. In general the spray angle reaches its maximum value at a given mass flow rate $\dot{M}$ and remains almost constant for subsequent increments of $\dot{M}$. By increasing the vapour pressure, the resulting force in the radial direction, responsible for the formation of the hollow cone, diminishes because of the higher resistance of the vapour against the liquid flow also causing a decrease in the spray angle. This observation agrees with the theory of Fraser and Eisenklam [17] for increments of the vapour pressure below a given limit. If the vapour pressure is incremented over that limit, the nozzle workwise changes as explained above. The emerging liquid occupies more volume than if discharged as a liquid sheet. For this reason, the spray angle increases again. For the studied nozzle, a vapour pressure of 0.25 MPa corresponded to the minimum spray angle at $\dot{M} > 2$ g s^{-1}. At pressures higher than 0.25 MPa, the spray angle behaves contrary to as expected, it varies directly proportional to the vapour pressure.

Condensation rate and heat transfer coefficient

The global condensation rate $\dot{M}_C$ on the spray can be expressed as the sum of the condensation rate on the liquid sheet $\dot{M}_S$ and on the droplet swarm $\dot{M}_D$, that is

$$\dot{M}_C = \dot{M}_S + \dot{M}_D \qquad (3)$$

in which the summands are evaluated separately as follows.

Heat transfer on the liquid sheet. The problem of the heat transfer on a conical liquid sheet was solved numerically by Lee and Tankin [2]. The authors assume an axis symmetrical, constant velocity profile in the liquid sheet and that the removal of heat from the interface is realized exclusively by conduction in the liquid. With these assumptions they reduced the energy balance on an infinitesimal annular element of the cone to the classic problem in transient conduction heat transfer. Following the results in ref. [2], the integrated form of the energy balance can be expressed in terms of the amount of vapour condensing on the liquid, which means the value of $\dot{M}_S$, one obtains

$$\dot{M}_S = \rho \pi \delta \bar{U} L_z \mu \tan\left(\frac{\alpha}{2}\right) - \dot{M} \qquad (4)$$

where ρ means the liquid density which is calculated by applying the 1/3 rule [21] and δ the mean sheet thickness. μ is defined by

$$\mu = \left[1 + \tan^2\left(\frac{\alpha}{2}\right)\right]^{1/2}.$$

With exception of δ, all parameters in equation (4) are known. δ could not be obtained directly from the holographic reconstructions. The cause of that lay in the very waved form of the liquid sheet as well as in the irregular appearance of perforations of different size and shape in the liquid sheet. All this made it difficult to obtain confident measurements of the sheet thickness. We overcame this situation by applying a recurrent procedure with the aid of the temperature measurements presented in Fig. 8. In a first approximation a value of δ is deduced by matching equation (4) with the equation of the ideal condensation

$$\dot{M}_S = \frac{c_p(T_{L_z} - T_0)\dot{M}}{h_{fg}} \qquad (5)$$

with

c_p specific heat of the liquid

h_{fg} latent heat of vaporization and

T_{L_z}, T_0 the temperatures defined in Fig. 1.

Later, this value is corrected by solving equation (3) after the calculation of $\dot{M}_D$. The value of the global condensation rate $\dot{M}_C$ in equation (3) is then obliged to match with the condition of total condensation

$$\dot{M}_C = \frac{c_p(T_{sat} - T_0)\dot{M}}{h_{fg}} \qquad (6)$$

by varying $\dot{M}_S$, from which a corrected value of δ is obtained. The assumption of total condensation in equation (6) is substantiated by temperature measurements on the liquid far away from the nozzle. At values of the axial coordinate $z > 96$ nozzle diameters the temperature T of the droplets was always identical
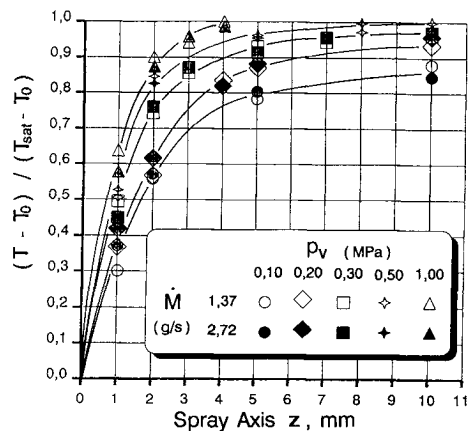

Fig. 8. Temperature measurements along the spray axis.

with the saturation temperature T_{sat} of the vapour environment. The values of the subcooling $\Delta T = T_{sat} - T_0$ can be obtained from Table A1 in the Appendix.

The variation of $\dot{M}_S$ as a function of the mass flow rate $\dot{M}$ at different vapour pressures p_v is presented in Fig. 9(a). In this diagram the upper limit of the mass flow rate range was restricted to 2.72 g s^{-1}, just around values of $\dot{M}$ at which the transition in the nozzle workwise occurs. $\dot{M}_S$ varies in direct proportion to the mass flow rate. With regard to the vapour pressure, we note a direct proportionality at $p_v < 0.4$ MPa. At higher pressures $\dot{M}_S$ decays in a similar way as the spray angle in Fig. 7(b) does. The lines in the diagram indicate the trend of the measured values.

The heat transfer coefficient h_S resulting from vapour condensation on the liquid sheet is obtained from the condition of heat flux continuity at the liquid sheet surface, that is

$$h_S = \frac{h_{fg}\dot{M}_S}{A_S(T_{l_c} - T_0)} \qquad (7)$$

where A_S means the surface of the liquid sheet deduced from equation (4). Both the outside and inside surfaces of the conical sheet were taken into account. h_S varies between 19 kW m^{-2} K (at $\dot{M} = 1.37$ g s^{-1} and

$p_v = 0.1$ MPa) and 256 kW m^{-2} K (at $\dot{M} = 2.72$ g s^{-1} and $p_v = 1.0$ MPa).

A diagram of the variation of h_S as a function of $\dot{M}$ for different vapour pressures p_v is shown in Fig. 9(b). One observes that for low vapour pressures the mass flow rate $\dot{M}$ influences very strongly the behaviour of the heat transfer coefficient, attenuating later at higher pressures. This behaviour of h_S can be cleared by relating it to the variation of the liquid sheet geometry (i.e. A_S) shown in Figs. 6(a) and (b). Particularly in Fig. 6(b) the influence of the mass flow rate attenuates at vapour pressures $p_v > 0.4$ MPa. In addition to that, the latent heat of vaporization h_{fg} diminishes with the increasing pressure p_v of the saturated vapour environment, such that the amount of heat to transfer diminishes too. Therefore, the heat transfer coefficient also decays at higher pressures.

Droplet growth. By applying the droplet measurement method, shown in Fig. 4, on single pulsed holograms taken at two different distances from the spray nozzle, a mean droplet growth is obtained. For a given mass flow rate $\dot{M}$ and vapour pressure p_v, two holograms, the first one centred on $z = 9$ nozzle diameters and the second one on $z = 96$ nozzle diameters, were recorded and evaluated. A statistical comparison of the measured droplet classes allowed for the evaluation of relative droplet size increments of the form

$$\delta D = \left[\frac{F(Di)}{F_{max}}\right]_f - \left[\frac{F(Di)}{F_{max}}\right]_n \qquad (8)$$

where Di means the drop size class, $F(Di)$ the frequency or repetition rate of drops of class Di, F_{max} the maximum frequence and the subindex f and n identify the far and the near spray regions, respectively. Typical measurements of the relative droplet growth δD in cumulative form $(\Sigma \delta D(Di))$ are shown in Fig. 10. First, one observes a decrease of the curves under the zero-line followed by an increase above the zero-line. If the droplets are supposed to be in a growing process, more little drops are found in the n-region than in the f-region leading to a negative slope of the cumulative growing curves. The little drops in the n-region do not disappear, they wander to the next higher drop size class in the f-region. They increase $F(Di)|_f$ with respect to $F(Di)|_n$ such that the curves smoothly change to a positive slope, raise over the zero-line and keep positive.
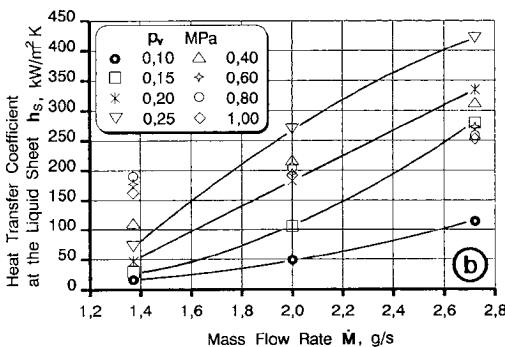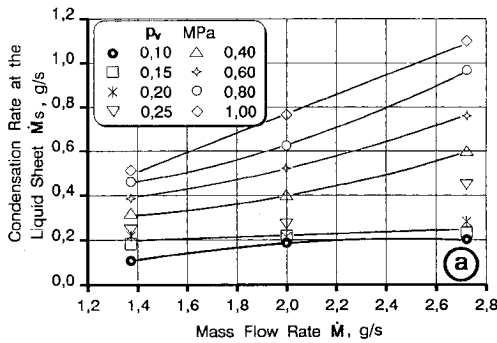

FIG. 9. (a) Condensation rate M_S and (b) heat transfer coefficient h_S at the liquid sheet of the R113 spray injected into its own saturated vapour at different vapour pressures p_v. They are represented as functions of the mass flow rate $\dot{M}$.
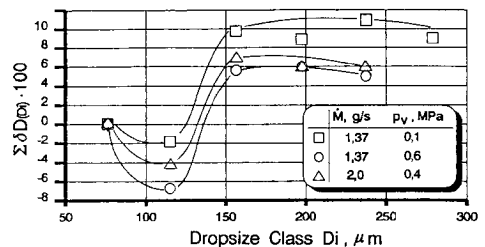

FIG. 10. Examples of the measurements of the relative droplet growth δD represented in cumulative form.

The final value of the curves in Fig. 10 multiplied with the mean droplet diameter $\bar{D}$ represents the mean droplet growth $\delta\bar{D}$ and is equivalent to the integral

$$\delta\bar{D} = 2\int_0^{t'} \dot{R}\,dt \qquad (9)$$

of the time resolved growth rate $\dot{R}$ known from the literature (e.g. see refs. [6, 8, 15]). Comprehensive data of the dropsize distributions for the near and far spray regions were published in ref. [20].

Expressing $\delta\bar{D}$ in the form

$$\frac{D}{D_0} = D_0 + D_0\delta\bar{D} \qquad (10)$$

where D means the actual drop diameter and D_0 the initial drop diameter, direct comparisons with data by other authors can be performed. Figure 11 shows an example in which our data are compared with the correlation presented by Ford and Lekic [8]. To build up their correlation the authors measured, by using high speed cinematography, the drop growth of single water drops falling free through a saturated steam environment. For the comparison we calculated the time scale of the heat diffusion in the R113 droplets by applying the Fourier analogy. The time scale relation was

$$t(R113) = 0.026t(\text{water}). \qquad (11)$$

Heat transfer on the droplets. Considering that

- the emerging liquid from the conical sheet distributes in spherical droplets of diameter equal to the Sauter mean diameter D_{32},
- the temperature on the drops surface is always equal to the vapour temperature T_{sat}, and
- they reach a uniform temperature equal to the saturation temperature in an interval Δt, which can be expressed as a multiple of the time $\Delta t'$ needed by a liquid particle to go from the nozzle exit up to the break up point,

the condensation rate $\dot{M}_D$ at the droplet swarm can be given by

$$\dot{M}_D = \frac{\rho-\rho_v}{\rho}\frac{3(\delta\bar{D}+\delta\hat{D})}{D_{32}}(\dot{M}+\dot{M}_S) \qquad (12)$$

where ρ_v means the density of the vapour and $\delta\hat{D}$ an idealized droplet growth corresponding to the liquid ligaments in the break up zone.

As total condensation is assumed at the centerpoint of the far spray region ($z = 96$ nozzle diameters), it is possible to calculate the condensation rate due only to $\delta\bar{D}$ between the centerpoints $z = 9$ and 96 nozzle diameters, with which the temperature T ($z = 9$) is calculated

$$\dot{M}_{D,2} = \frac{\rho-\rho_v}{\rho}\frac{3(\delta\bar{D})}{D_{32}}(\dot{M}+\dot{M}_S+\dot{M}_{D,1}) \qquad (13)$$

with $\dot{M}_{D,1}$ the condensation rate due to $\delta\bar{D}$. Assuming then ideal condensation between $z = L_z$ and 9, $\dot{M}_{D,1}$ results

$$\dot{M}_{D,1} = \frac{c_p[T(z=9)-T_{L_z}]}{h_{fg}}(\dot{M}+\dot{M}_S) \qquad (14)$$

from which $\delta\bar{D}$ can be calculated and hence equations (13) and (12) can be solved to give the condensation rate at the droplet swarm $\dot{M}_D$. The results of this evaluation are shown in the diagram in Fig. 12(a), in which we note the influence of the spray geometry. As the droplets can only collect the residual heat, which could not be collected by the liquid sheet, the condensation rate $\dot{M}_D$ behaves complementary to $\dot{M}_S$ at
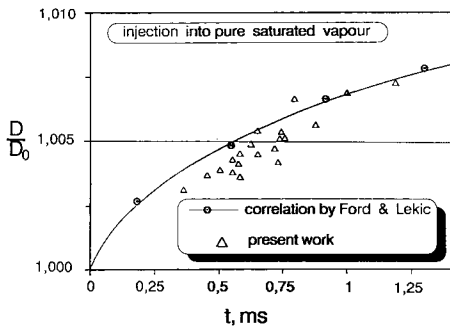
FIG. 11. Comparison of the holographically measured droplet growth with results by Ford and Lekic [8]. Note that the triangles represent mean values obtained from some thousands of droplets while the circles describe measurements on a single droplet.
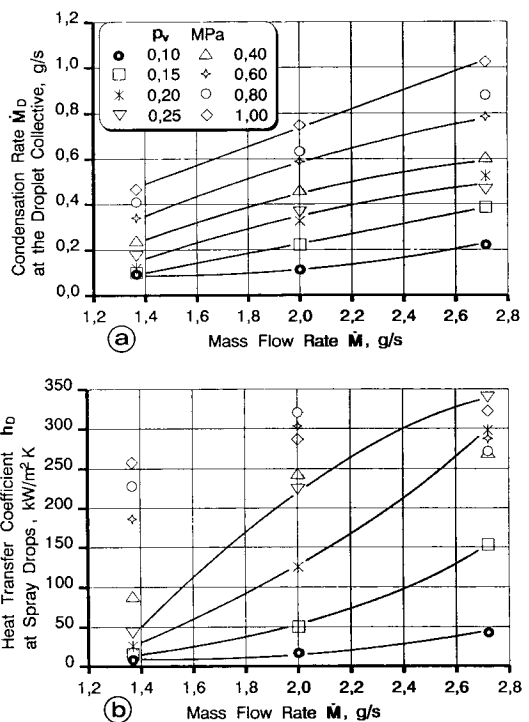
FIG. 12. (a) Condensation rate $\dot{M}_D$ and (b) heat transfer coefficient h_D at the droplet zone of the R113 spray injected into its own saturated vapour at different vapour pressures p_v.

vapour pressures $p_v < 0.4$ MPa. At higher pressures the influence of the spray geometry slowly disappears and both $\dot{M}_D$ and $\dot{M}_S$ behave similarly.

The heat transfer coefficient h_D resulting from the vapour condensation on the droplets is obtained by applying the condition of continuity of heat flux at the interface between the droplets and their vapour environment, that is

$$h_D = \frac{h_{fg}\dot{M}_D}{N\pi(D_{32})^2[T_{sat} - T_{L}]} \quad (15)$$

with N as the amount of drops

$$N = \frac{6V_s}{\pi(D_{32})^3} \quad (16)$$

resulting from the liquid sheet volume V_s. h_D varies in this case between 5 and 325 kW m^{-2} K. Figure 12(b) shows the behaviour of the heat transfer coefficient as a function of the mass flow rate $\dot{M}$ at different vapour pressures p_v. The trend of the data is very similar to that for the case of the heat transfer coefficient h_S in Fig. 9(b).

Dimensionless representation of the measured data. In order to use the results of this work for estimations of the behaviour of other fluids when they are injected into their own saturated vapour at raised saturation pressures, we present an example of the variation of the Nusselt number

$$Nu = \frac{h_D\bar{D}}{\lambda} \quad (17)$$

as a function of the droplet Reynolds number

$$Re = \frac{\rho_v\bar{U}\bar{D}}{\eta_v} \quad (18)$$

for a mass flow rate of $\dot{M} = 1.37$ g s^{-1} in Fig. 13. There we observe clearly the effect of varying the vapour pressure. At a constant mass flow rate, the pressure p_v alone causes dramatic changes not only on the heat transfer but also on the hydrodynamics of the spray flow.
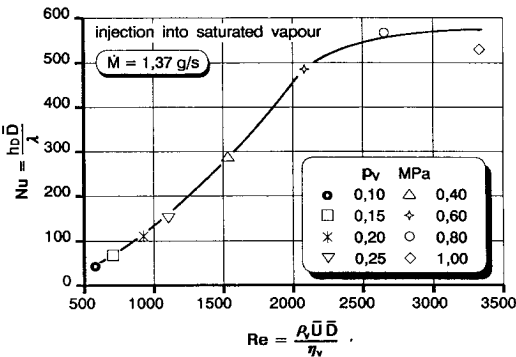
Representing the physical properties of the fluid and the subcooling ΔT through the Jakob number

$$Ja = \frac{c_p\rho(T_{sat} - T)}{\rho_v h_{fg}} \quad (19)$$

and correlating it with the Reynolds number and the mass flow rate expressed in the form of a reference Reynolds number

$$Re_0 = \frac{\dot{M}}{\eta_0 d_0} \quad (20)$$

where η_0 means the viscosity of the liquid at 25°C and d_0 the bore diameter of the nozzle, we found the relation

$$Re^{1/3} Ja = 32 Re_0^{1/4} \quad (21)$$

to describe the dynamic of the fluid flow which represents the measured data between an uncertainty of 8%. Equation (21) describes a family of straight lines in which each line represents a constant vapour pressure. Figure 14 shows equation (21) graphically. The dashed lines indicate the region in which the spray is still in development.

UNCERTAINTIES

Uncertainty in the evaluation of the holograms

The main source of uncertainty in the measurement method lies in the pixel representation of circular objects (droplets), especially when these objects contain less than 10 pixels (independent of the absolute pixel size). By setting the resolution of the area measurement method to 5 pixels, a maximum error of $\pm 3\%$ was obtained by comparing a circular area with a pixel ensemble in which the amount of pixels was varied between 6 and 40 pixels. In this work, the smallest drop images contain 6 pixels ($\phi60$ μm) and the largest ones 148 pixels ($\phi300$ μm). For larger objects or structures, the error is less than 1%.

Uncertainty in the heat transfer measurement

In this case the uncertainty is much more higher than for the hologram evaluation. There are two major error sources:

(a) the statistical error E_S which is represented by the standard deviation being of the order of 7% and

FIG. 13. Nusselt number as a function of the droplet Reynolds number for a constant mass flow rate of $\dot{M} = 1.37$ g s^{-1} and different vapour pressures p_v.
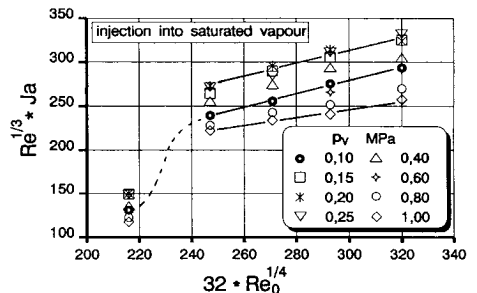

FIG. 14. Behaviour of the dimensionless group $\{Re^{1/3} Ja\}$ as a function of the reference Reynolds number Re_0.

Measurement of direct-contact condensation of pure saturated vapour

(b) the error E_T in the measurement of the bulk liquid temperature, which is inversely proportional to the subcooling ΔT, from 5% at $\Delta T > 20$ K up to 30% at $\Delta T \approx 1$ K.

The statistical error directly affects the measurement of the droplet growth, i.e. the heat transfer to the droplets, and indirectly the computation of the heat transfer to the liquid sheet, because of our recursive scheme to calculate the mean sheet thickness $\bar{\delta}$. As the temperature measuring error also affects the measurement of the heat transfer in both spray zones, the maximum relative error E_{max} in the condensation rate and evaluation of the heat transfer coefficient, calculated through the logarithmic differential of equations (3), (4), (7), (12) and (15) resulted in the range of 8% to 23%.

CONCLUSION

From the presented results we can conclude that the injection of subcooled liquids, though pressure-swirl nozzles, into saturated vapour atmosphere, at increased pressures, reach completely new dimensions than those at low vapour pressure as known from the literature. This influences not only the behaviour of the injection spray, but also the heat and mass transfer caused by condensation. The heat transfer increases no longer with the increasing liquid velocity. Instead of that, it approximates asymptotically to its maximum value. Design of injection facilities thought to work at high vapour pressures has therefore to take into account the effect of the high pressure upon the dynamics of the fluid flow and upon the direct-contact condensation.

REFERENCES

1. A. Lekic and J. D. Ford, Direct contact condensation on a spray of subcooled liquid droplets, *Int. J. Heat Mass Transfer* **23**, 1531–1537 (1980).
2. S. Y. Lee and R. S. Tankin, Study of liquid spray (water) in a condensable environment (steam), *Int. J. Heat Mass Transfer* **27**, 363–374 (1984).
3. K. Hijikata, Y. Mori and S. Kawaguchi, Direct contact condensation of vapour on falling droplets, *Int. J. Heat Mass Transfer* **27**, 1631–1640 (1984).
4. G. P. Celata, M. Cumo, F. D. Annivale and G. E. Farello, Direct contact condensation of steam on droplets, *Int. J. Multiphase Flow* **17**, 191–211 (1991).
5. T. Richter and P. Walzel, Zerstäuben von Flüssigkeiten mit Hohlkegeldüsen, *Chem.-Int.-Tech* **61**(4), S. 319–321 (1989).
6. T. Sundararayan and P. S. Ayyaswamy, Heat and mass transfer associated with condensation of a moving drop: solutions for intermediate Reynolds numbers by a boundary layer formulation, *ASME J. Heat Transfer* **107**, 409–415 (1984).
7. T. Sundararayan and P. S. Ayyaswamy, Hydrodynamics and heat transfer associated with condensation on a moving drop: solutions for intermediate Reynolds numbers, *J. Fluid Mechanics* **149**, 33–58 (1985).
8. J. D. Ford and A. Lekic, Rate of growth of drops during condensation, *Int. J. Heat Mass Transfer* **16**, 61–64 (1973).
9. E. Kulic and E. Rhodes, Heat transfer rates to moving droplets in air–steam mixtures, *6th Int. Heat Transfer Conf.*, Ontario, Vol. 2, pp. 464–474 (1978).
10. E. Kulic, E. Rhodes and G. Sullivan, Heat transfer rate predictions in condensation on droplets from air–steam mixtures, *Can. J. Chem. Engng* **53**, 252–258 (1975).
11. J. N. Chung, P. S. Ayyaswamy and S. S. Sadhal, Laminar condensation on a moving drop. Part 1: singular perturbation technique, *J. Fluid Mech.* **139**, 105–130 (1984).
12. P. O. Brunn, Heat and mass transfer from single spheres in a low Reynolds number flow, *Int. J. Engng. Sci.* **7**, 817–822 (1982).
13. J. N. Chung and P. S. Ayyaswamy, Material removal associated with condensation on a droplet in motion, *Int. J. Multiphase Flow* **7**, 229–242 (1981).
14. J. N. Chung, P. S. Ayyaswamy and S. S. Sadhal, Laminar condensation on a moving drop. Part 2: numerical solutions, *J. Fluid Mech.* **139**, 131–144 (1984).
15. L. J. Huang and P. S. Ayyaswamy, Heat and mass transfer associated with a spray drop experiencing condensation: a fully transient analysis, *Int. J. Heat Mass Transfer* **30**, 881–891 (1987).
16. S. M. De Corso and G. A. Kemeny, Effect of ambient and fuel pressure on nozzle spray angle, *Trans. ASME* **79**, 607–615 (1957).
17. R. P. Fraser and P. Eisenklam, Liquid atomization and the drop size of sprays, *Trans. Instn Chem. Engrs* **34**, 294–319 (1956).
18. A. Chávez and F. Mayinger, Single- and double-pulsed holography for the characterization of sprays of refrigerant R113 injected into its own saturated vapor. In *Experimental Heat Transfer, Fluid Mechanics and Thermodynamics* (Edited by R. K. Shah, E. N. Ganic and K. T. Yang), pp. 848–854. Elsevier, Amsterdam (1988).
19. A. Chávez and F. Mayinger, Evaluation of pulsed laser holograms of spray droplets by applying digital image processing, *Proc. 9th Int. Conf. on Heat Transfer*, Jerusalem 19–24 August, pp. 187–192. Hemisphere, New York (1990).
20. A. Chávez, Holografische Untersuchung an Einspritzstrahlen–Fluiddynamik und Wärmeübergang durch Kondensation–, Dissertation, T.U. München (1991).
21. G. L. Hubbard, V. E. Denny and A. F. Mills, Droplet evaporation: effects of transients and variable properties, *Int. J. Heat Mass Transfer* **18**, 1003–1008 (1975).

APPENDIX

Table A1. Liquid refrigerant R113 injected into its own saturated vapour

p_{sat} MPa	T_{sat} °C	\(\dot{M}\) (g s^{-1}) 0.80	1.37	2.00 T_0, °C	2.72	3.86
0.10	47.7	33.4	26.8	25.5	24.8	24.1
0.15	60.0	39.3	29.7	27.8	26.7	25.7
0.20	69.7	44.6	33.0	30.7	29.4	28.2
0.25	77.7	49.3	36.1	33.5	31.9	30.6
0.30	84.6	53.4	38.9	36.0	34.3	32.8
0.40	96.1	60.3	43.8	40.4	38.5	36.8
0.50	105.6	66.2	47.9	44.3	42.1	40.3
0.60	113.8	71.2	51.5	47.6	45.3	43.3
0.70	121.1	75.8	54.8	50.6	48.2	46.0
0.80	127.6	79.8	57.7	53.3	50.7	48.4
0.90	133.6	83.5	60.4	55.8	53.1	50.7
1.00	139.0	86.9	62.8	58.0	55.2	52.7

Measured values of the initial temperature T_0 at the nozzle outlet at different conditions of mass flow rate $\dot{M}$ and saturation pressure p_{sat}. The values of the saturation temperature T_{sat} are included for reference.

L'APPLICATION DE L'HOLOGRAPHIE LASER ULTRA-RAPIDE A LA MESURE DE LA CONDENSATION DIRECTE A JETS DANS UNE ATMOSPHERE DE LA VAPEUR SATUREE

Résumé—Une application de l'holographie laser ultra-rapide à la mesure de la croissance des gouttelettes de jets sous-refroidis dans une vapeur saturée est présentée. L'écoulement du jet correspond à des nombres de Reynolds de gouttelettes intermédiares et élevés ($100 \leqslant Re \leqslant 3500$), tandis que la pression de la vapeur varie dans un large domaine de pression réduite ($0,03 \leqslant p_r \leqslant 0.3$). Les reconstructions holographiques ont révélé un lien important entre la pression de vapeur et la géométrie du jet. Pour un débit liquide modéré et une pression de vapeur relativement élevée, une augmentation ultérieure de la pression produit des changements radicaux dans la géométrie du jet et réduit considérablement le taux de condensation.

ANWENDUNG DER IMPULSHOLOGRAFIE ZUR MESSUNGEN DER DIREKT-KONDENSATION AN EINSPRITZSTRAHLEN IN REINER SATTDAMPFATMOSPHÄRE

Zusammenfassung—Eine Anwendung der Impulsholografie zur direkten Messungen der Größenzunahme von Tropfen aus unterkühlten Einspritzstrahlen in reiner Sattdampfatmosphäre wird dargestellt. Die Flüssigkeit wurde unterkühlt bei verschiedenen Massenströmen eingespritzt, die einem Bereich von mäßigen bis hohen Tropfen-Reynolds-Zahlen ($100 \leqslant Re \leqslant 3500$) entsprachen. Dabei wurde der Dampfdruck im Einspritzraum in einem breiteren Bereich von reduzierten Drücken ($0,03 \leqslant p_r \leqslant 0,3$) variiert. Die holografischen Rekonstruktionen zeigen eine sehr starke Beziehung zwischen dem Dampfdruck und der Strahlgeometrie. Bei mäßigen Massenströmen und relativ hohen Dampfdrücken, rufen weitere Druckerhöhungen drastische Änderungen in der Strahlgeometrie hervor, die eine Verminderung der Kondensationsrate zu Folge haben.

ИССЛЕДОВАНИЕ КОНДЕНСАЦИИ ПРИ НЕПОСРЕДСТВЕННОМ КОНТАКТЕ ЧИСТОГО НАСЫЩЕННОГО ПАРА И РАСПЫЛА МЕТОДОМ ИМПУЛЬСНОЙ ЛАЗЕРНОЙ ГОЛОГРАФИИ

Аннотация—Описывается использование импульсной лазерной голографии при прямом измерении роста недогретых капель распыла в чистом насыщенном паре. Течение распыла соответствует промежуточным и высоким числам Рейнольдса для капель ($100 \leqslant Re \leqslant 3500$), в то время как давление пара изменяется в широком диапазоне приведенных давлений ($0,03 \leqslant p_r \leqslant 0,3$). Голографические исследования обнаружили наличие сильной взаимосвязи между давлением пара и геометрией распыла. При умеренном расходе жидкости и относительно высоком давлении пара последующий рост давления приводит к существенным изменениям геометрии распыла и значительному снижению интенсивности конденсации.